Experimental study on the contact angle formation of solidified iron–chromium droplets onto yttria ceramic substrates for the yttria/ferrous alloy system with variable chromium content

K. Verhiest[a,f,g,*], S. Mullens[b], J. Paul[c], I. De Graeve[d], N. De Wispelaere[e], S. Claessens[e], A. DeBremaecker[f], K. Verbeken[g]

[a]ArcelorMittal Gent, Hot Strip Mill Department, J. Kennedylaan 51, 9042 Ghent, Belgium
[b]Flemish Institute for Technological Research, VITO, Materials Technology, Boeretang 200, 2400 Mol, Belgium
[c]Flanders Materials Centre, Flamac, Technologie Park 903, 9052 Ghent, Belgium
[d]Vrije Universiteit Brussel, VUB, Pleinlaan 2, 1050 Brussel, Belgium
[e]ArcelorMittal Research Industry Gent, OCAS, J. Kennedylaan 3, 9060 Zelzate, Belgium
[f]Belgian Nuclear Research Centre, SCK•CEN, Boeretang 200, 2400 Mol, Belgium
[g]Ghent University, UGent, Department of Materials Science and Engineering (DMSE), Technologie Park 903, 9052 Ghent, Belgium

Abstract

High-temperature contact angle experiments of liquid iron–chromium (Fe–Cr) drops onto ceramic yttria (Y_2O_3) substrates were carried out in order to investigate the wetting behavior of Y_2O_3 nano-particles in contact with an iron melt containing elemental Cr. Therefore, the correlation between the wetting behavior of the iron drop in contact with Y_2O_3 was studied for drops with variable Cr-content and for different powder grades. The wetting behavior of liquid binary Fe–Cr alloys in contact with the Y_2O_3 ceramic substrates at high temperature, was investigated using the static sessile drop method. The contact angle formed at the interaction interface was evaluated using static drop imaging and quantified using the method proposed by Bartlett and Hall [10].

Our experiments demonstrate that the wetting behavior of binary Fe–Cr alloys drops in contact with Y_2O_3 ceramics compared to other oxides such as Al_2O_3, is quite weak. Only for the test condition of pure electrolytic iron, i.e., without Cr addition, the contact angles (θ_c) were found to approach $90°$ or lower in all cases. Furthermore, a 9 wt% Fe–Cr alloy with silicon addition seems to improve the wetting behavior of liquid Fe–Cr drops in contact with Y_2O_3. Moreover, variation in powder purity seems to be of crucial importance.
© 2013 Elsevier Ltd and Techna Group S.r.l. All rights reserved.

Keywords: Melt phase; Iron–chromium alloy; Ceramic oxides; Wettability; Contact angle

1. Introduction

In literature, the wetting behavior for ceramic systems has been studied thoroughly for all kinds of materials: glasses; liquid metals (low-melting as well as high-melting); low-melting liquid oxides in contact with solid refractory or (non)-oxide substrates [1–16]. Bartlett and Hall have reported

wetting phenomena at the solid/liquid (S/L) interface for ceramic systems, with a special emphasis on the wetting behavior of high-melting liquid oxides (e.g., Al_2O_3) in contact with different solids [10].

Wetting ability, often briefly stated as wett-ability between a liquid (L) phase in contact with a solid (S) surface can be briefly described as the ability of bonding or adherence between both phases at the point of interfacial contact. The degree of contact between the liquid and the solid surface is determined by the resultant of adhesive and cohesive forces which finds its primary cause in the intermolecular interactions between solid and liquid. During spreading wetting, the final interplay of adhesive and cohesive forces at the S/L interface

*Corresponding author at: ArcelorMittal Gent, Hot Strip Mill Department, J. Kennedylaan 51, 9042 Ghent, Belgium. Tel.: +32 9 347 23 10; fax: +32 9 347 49 78.

E-mail addresses: Katelijne.Verhiest@arcelormittal.com, ktlne@yahoo.com (K. Verhiest).

causes the liquid to spread across the solid surface in case of strong adherence or wetting or causes the liquid drop to ball-up avoiding as much contact as possible in case of non-wetting. The degree of wetting contact is quantified through the contact angle (θ_c) formed at the S/L interface.

The contact angle is inversely related to the degree of wetting, meaning that strong wettability implies a low contact angle, i.e., a θ_c varying between $0°$ and $90°$. In case of weak wettability, the contact angle value exceeds $90°$, meaning that the fluid will minimize its contact area with the solid surface, consequently with the formation of a compact liquid droplet.

In case of spreading wetting, Young's equation states that θ_c is mathematically related to the surface energy vectors γ_{SL}, γ_{SV} and γ_{LV} formed at the contact interfaces [10,17].

For a system in thermodynamic equilibrium ($\Delta G=0$) the equation referred to as the Young's equation, is given by the following equation [17]:

$$\gamma_{SL}-\gamma_{SV} = -\gamma_{LV}\cos\theta_c \tag{1}$$

The droplet is subjected to capillary forces, as well as hydrostatic pressures. Equating both the Laplace pressure γ/κ^{-1} and the hydrostatic pressure $\rho g\kappa^{-1}$ for a liquid with density ρ and the acceleration due to gravity ($g=9.8$ m/s^2), the capillary length is defined as the characteristic length above which gravity forces become important, illustrated by the following equation:

$$\kappa^{-1} = \sqrt{\frac{\gamma}{\rho g}} \tag{2}$$

The surface energy and consequently the contact angle can be influenced by various experimental parameters such as variation in exposure time and temperature as well as surface substrate conditions. Many metal/ceramic couples are far from equilibrium and the resulting interfacial reactions can strongly modify the chemistry, structure and topography of the contact area [13]. Reactive wetting can be of great influence in the control of spreading wetting and on the final formation of the contact angle at the metal/oxides interface during high-temperature exposure, post-wetting parameters (post-solidification and cooling speed), resulting in lower or increased wettability [1]. The addition of active metals to the liquid drop phase can promote wetting of ceramics through the formation of a reaction product at the ceramic/metal interface. In several studies it is seen that metals in contact with ceramics exhibit obtuse contact angles, due to lower wettability towards ceramic materials. The activity of Cr added to the drop phase, resulting often typical in segregation phenomena, resulting in improved or decreased wettability, are seen at the interface area between solidified metal droplet and oxides substrates [18,19].

Up till now, in case the production of high-temperature creep resistant steels or the so-called advanced creep and corrosion resistant steels, those particular studies can be of considerable practical interest to understand the wettability behavior of nano-Y_2O_3 particles when added to a steel melt. Oxides dispersion strengthened (ODS) steels are of particular interest in the energy community for their application as long-life core structural materials in nuclear fusion and fission reactors [20–27]. Although

the materials composition is well-known for its nuclear application, it is also envisaged for application in classic steam and gas power production units [28].

Within the framework of this study, we report on the wetting behavior between high-melting binary iron–chromium (Fe–Cr) alloys and high-melting Y_2O_3 solids. Chromium-content of the alloy is varied between 0 and 20 wt%, additionally 0.5 wt% Si is added to the 9 wt% Fe–Cr alloy. In this work, as-obtained Y_2O_3 powder, with variation in purity, is characterized and prepared as workable substrates in order to perform contact angle experiments. The contact angle θ_c is determined using the sessile drop method. The contact angle is determined after drop solidification and quantified through the method proposed by Bartlett and Hall, as discussed below. OSM and EPMA is used to understand the chemical reactions playing at the interaction interface of contact angle formation. The final goal of the complete study is the production of yttria–ferrous systems as is detailed elsewhere [29,30]. In a first step, this work presents a screening on the wettability and contact angle formation for the Y_2O_3/Fe–Cr system. In order to investigate if gravitational forces are of influence during contact angle formation, the contact length is determined experimentally based on the contact angle drop images. Furthermore, reaction mechanisms responsible for the observed wetting behavior at the interaction interface for the yttria/ferrous alloy system with increased Cr-content are identified, within the experimental conditions detailed.

2. Experimental procedure

2.1. Powder characterization

Fine high-purity Y_2O_3 nano-powder (grade A, particle size < 100 nm) as well as impure Y_2O_3 nano-powder (purity < 99.6 wt%, particle size < 50 nm) was obtained.[1] The morphology of the as-obtained Y_2O_3 nano-powder has been verified using a field emission gun scanning electron microscope (FEG-SEM) type JEOL JSM-6340F (JEOL Ltd., Japan). The as-obtained powder size communicated by the manufacturer was verified on its size aberrations using a centrifugal particle sizing (CPS) disc centrifuge DC24000 (CPS Instruments Inc., Benelux Scientific). For the sake of clarity, in this work, the high-purity Y_2O_3 nano-powder will be abbreviated as powder P_1, the low-purity Y_2O_3 powder as powder P_2. Elemental purity of both Y_2O_3 powders was investigated with ICP-MS using a Thermo Finnigan ICP-MS Element II device, medium resolution (Thermo Finnigan Mat GmbH, Germany).

2.2. Ceramic substrates preparation

2.2.1. Powder densification

For contact angle measurements, all as-obtained Y_2O_3 nano-powders were compacted into cylindrical shaped samples using an uni-axial press type RP16 (Jenny Pressen, Switzerland) under

---

[1]For reasons of confidentiality, producer and production process of the powder are not given in this study. Purity grade values, as well as particle size indications in the text are provided by the manufacturer.

pressure loads of maximum 150 MPa. The finished diameter-to-height ratio of the cylindrical bodies was 10. After pressing the substrates, the cylindrical samples were densified during iso-thermal calcination under air in a Nabertherm furnace type HT166/17LB (Nabertherm GmbH, Germany). The sintering cycle involved a two-stage heating treatment. The first step ranging from room temperature to 1000 °C, followed immedi-ately by a second cycle ranging from 1000 °C to maximum sintering temperatures of 1700 °C at a heating ramp of 300 °C/h and 100 °C/h, respectively. After heating, the ceramic samples were kept for a specific time at a sintering temperature ranging from 1500 °C to maximum 1700 °C, followed by cooling down to room temperature at a cooling rate of 180 °C/h. For the remaining experiments described in the following of the text, in all cases the most optimal sample sintering condition (1600 °C —2 h) has been used.

2.2.2. Surface roughness

Apart from determination of the particle size distribution (PSD), high resolution FEI-XL30 scanning electron micro-scopy FEI-XL30 SEM (FEI Company, USA) was used to characterize the surface roughness of the powder P_1. After sintering and consequently before performing the contact angle experiments, the substrate surface was ground and polished with diamond paste (polish paste grain size 9 and 30 µm) in order to control the roughness at the S/L interface. From a theoretical point of view, the powder surface roughness factor (R_s) is defined as the ratio of the powder's real surface area (S_r) and geometric surface area (S_g) [31] R_s can be calculated by the following equation:

$$R_s = \frac{S_r}{S_g} \qquad (3)$$

The geometric surface area of a particle appearing in the formula for surface roughness calculations is inversely related to its density ($\rho_{Y_2O_3} = 5.03$ g/cm^3) [32] and particle diameter (D), and can be expressed by Eq. (4) [31]. For all calculations made with respect to the surface roughness of the nano-powder, the average value of D_{50} (50% statistical fraction in weight percent) obtained with CPS is used as particle diameter D.

$$S_g = \frac{6}{\rho D} \qquad (4)$$

2.2.3. Powder shrinkage

In order to investigate the Y_2O_3 powder shrinkage during high-temperature treatments, horizontal powder dilatometry (HPD) was performed using a Netzsch dilatometer 402C (Netzsch Instruments N.A. LLC., Burlington USA). For dilatometrical investigations, the powders P_1 and P_2 were pressed into cylindrical pastilles with volumes of 377 mm^3 and 267 mm^3, respectively. The heating cycle during HPD involved heating at a speed of 2.98 °C/min, holding at sintering temperatures of 1600 °C for a sintering time of 2 h, followed by cooling down to room temperature at a rate of

28.13 °C/min. After sintering, densities were determined gravimetrically.

2.3. Iron–chromium castings

Iron–chromium (Fe–Cr) alloys with increased Cr-content (0–2.5–5–9–12–14–20 wt% Cr) were produced under protec-tive argon atmosphere using a levitation casting device type Alu C1—1 × 400kVar MOSFET Transistors generator type GTM 12 HF (CELES, France). For the production of the Fe–Cr alloys, pure electrolytic iron was used as matrix material. Elemental impurities in the Fe–Cr castings were detected with inductively coupled plasma-mass spectroscopy (ICP-MS) using a Thermo Finnigan ICP-MS Element II, medium resolution equipment (Thermo Finnigan Mat GmbH, Germany). In order to investigate the influence of increased silicon (Si)-content on the wettability behavior between liquid Fe–Cr alloys and Y_2O_3 nano-powder, 0.5 wt% Si was added to the Fe–Cr alloy containing 9 wt% Cr. For contact angle wetting experiments, the Fe–Cr casts were sub-sectioned into small blocks dimensioned $5 \times 5 \times 2$ mm^3. The steel samples were polished oxide free by grinding.

2.4. Wettability

2.4.1. Experimental set-up

The ceramic Y_2O_3 substrates, prepared for wettability experi-ments, were loaded in a high-temperature furnace working under protective atmosphere, type Centorr/TORVAC M60-8 × 12-W-A-TMP4-0 (Cambridge Vacuum Engineering, United Kingdom). An alumina plate served as support for the ceramic substrates in contact with the metallic alloy. The experiments were elaborated under vacuum atmosphere (5×10^{-5} mbar) or under argon pressure (1125.48 mbar). A temperature of 1538 °C is required in order to sustain the melt phase, as illustrated by the binary Fe–Cr phase diagram simulated using Calphad calculations are presented in Fig. 1 [33].

A preliminary test with compressed alumina (Al_2O_3) sub-strates was done under vacuum and argon atmosphere in order
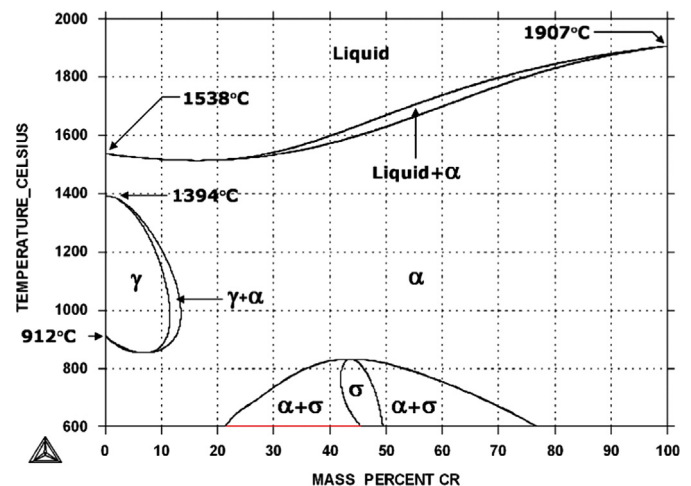

Fig. 1. Fe–Cr binary phase diagram based on Calphad simulations [33].
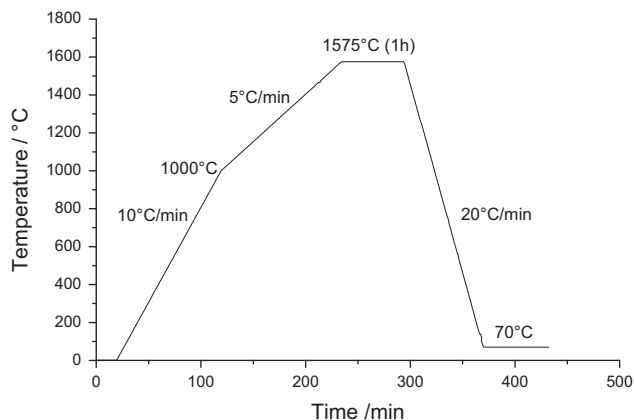
Fig. 2. Schematics of the performed heating cycle.

to outline the experimental set-up as well as to determine the experimental temperature window of interest. The programmed heating and cooling cycle applied during contact angle measurements are presented in Fig. 2.

Due to the observed fluctuations in the temperature profile between the solid loads temperature and the indicated furnace temperature, the working temperature was chosen about 40 °C above the required temperature, 1538 °C. After determination of the optimal working temperature, two high-temperature runs at 1575 °C (1848 K) were done under argon atmosphere for the seven Fe–Cr compositions and for the Si-added material in contact with Y_2O_3 pressed-substrates prepared with powders P_1 and P_2.

By seeing other studies of metal/oxides systems where Cr was added to the drop phase, exposure time of 1 h at elevated temperature should be sufficient [19]. The exposure temperature chosen (1575 °C) was in accordance with the envisaged industrial melting temperatures. The cooling down cycle is at the fastest rate being possible, in order to avoid post-phenomena.

2.4.2. Contact angle determination

The contact angle θ_c was quantified after solidification of the liquid Fe–Cr drop making contact with the ceramic Y_2O_3-substrate. For surface characterization, the ceramics with solidified drop were loaded in the cold state in a contact angle goniometer FTA 2000 (First Ten Ångströms Inc., Virginia). The shape or profile of the droplet was captured using an optical sub-system. With the method of Bartlett and Hall, flattening of the spherical curved side of the solidified droplet caused by gravitational forces is not taken into account. To verify if gravitational effects can be neglected against capillary forces, the capillary lengths (CL) were verified experimentally based on the solidified droplet images. The drop images for the yttria powder (P_1 and P_2) or alumina in contact with Fe–(0–20 wt% Cr) are presented in Fig. 3.

The contact angle θ_c can be derived from the method proposed by Bartlett and Hall i.e., by solving Eq. (4) in case of the conditions $\theta_c < 90°$ and $\theta_c > 90°$, respectively. The method proposed by Bartlett and Hall using equation Eq. (5) is justified since small drops were formed during contact angle

wetting and spherical drop formation was checked.

$$\begin{cases} \theta_c = \sin^{-1}\left(\frac{yx}{\frac{x^2}{4}+y^2}\right); & \theta_c < 90° \\ \theta_c = 90 + \tan^{-1}\left(\frac{y}{x}\right); & \theta_c > 90° \end{cases} \quad (5)$$

The goniometric parameters x and y can be determined using static sessile drop imaging presented schematically in Fig. 4.

2.4.3. Substrate analysis

Optical stereo microscopy (OSM) has been used to visualize the colorization of the Y_2O_3 ceramic substrates after air sintering the basic ceramic substrates, for both impure and pure Y_2O_3 powder. After contact angle measurements, OSM was used to re-depict the colorization of the Y_2O_3 substrates. For OSM imaging, an optical stereo microscope Leica MZ125 pixeLINK camera inclusive, combined with software analysis (Olympus) has been used. No special sample treatment was needed on the sintered samples in order to perform OSM.

2.4.4. Reaction chemistry

In combination with OSM, electron probe micro analysis (EPMA) was performed in order to investigate the reaction chemistry occurring at the S/L interface where the solidified steel drop makes contact with the Y_2O_3 ceramic. EPMA measurements were performed using a device Microlab32 (Jeol, Japan). The selection of the samples for EPMA was done with the intention to investigate the effect of the increased amount of Cr as well as the addition of Si. Elemental mapping is done for both Y_2O_3 powders in contact with Fe–9 wt% Cr (+0.5 wt% Si) alloys. Fig. 5 presents a back-scattered electron (BSE) image of the interfacial zone selected for EPMA measurements after contact angle wetting between Y_2O_3 ceramic and a liquid Fe–Cr drop, with special emphasis for P_2/Fe–9 wt.% Cr (Fig. 5(a)) and for P_2/Fe-9 wt.% Cr–0.5 wt.% Si alloys (Fig. 5(b)).

3. Results and discussion

3.1. Particle size distribution

Fig. 6 presents the cumulative frequency distribution curves observed using CPS for the as-obtained Y_2O_3 nano-powders P_1 and P_2.

From the cumulative frequency curves presented in Fig. 6 it can be derived that the statistical fractions D_{10}, D_{50} and D_{90} are 0.1, 0.4 and 0.7 μm respectively for powder P_1; and 0.2, 0.4 and 0.9 μm for powder P_2. From those observations it can be seen that the average particle size deviates significantly from the value indicated and provided by the manufacturer, i.e., the individual particles tend to agglomerate strongly instead of being individually separated. Agglomeration tendency is a well-known difficulty in the production of nano-powder and often described in literature [34,35]. Fig. 7 depicts SEM-images of the as-obtained powders P_1 and P_2 confirming the agglomeration state of the individual nano-sized Y_2O_3 particles as well as their spherical morphology.
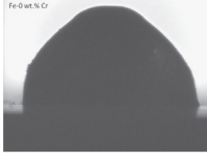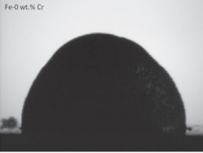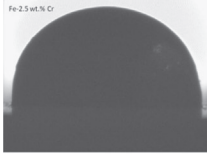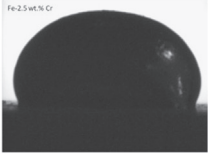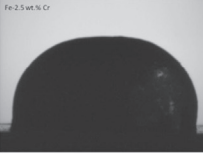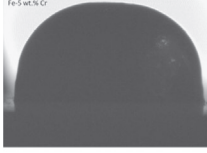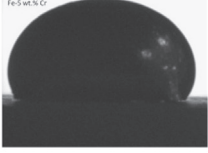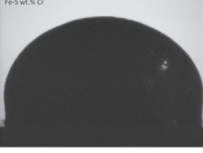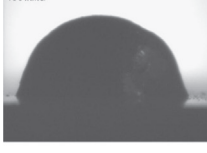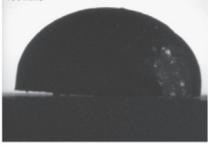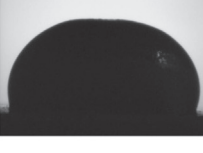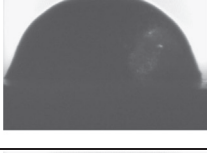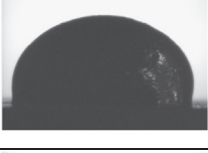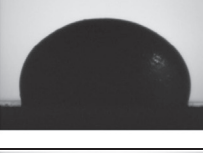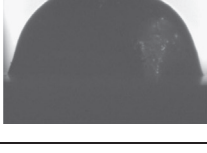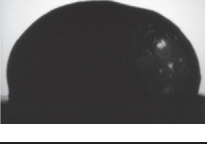
Oxide/Ferrous alloy	Al$_2$O$_3$	P1 Y$_2$O$_3$	P2 Y$_2$O$_3$
Fe			
Fe-2.5wt.Cr			
Fe-5wt.Cr			
Fe-9wt.Cr			
Fe-12wt.Cr		N.A.	
Fe-14wt.Cr			
Fe-20wt.Cr			

Fig. 3. Contact angle wetting images of Fe–(0–20 wt% Cr) droplets in contact with alumina and yttria P$_1$ and P$_2$ pressed substrates.
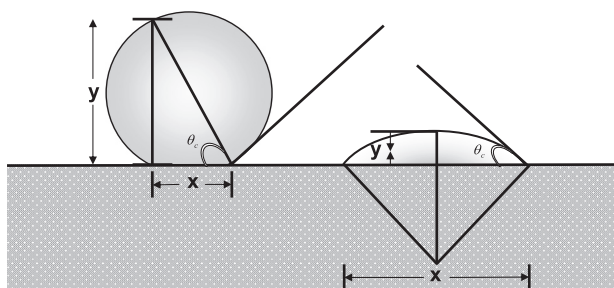
Fig. 4. Contact angle θ_c determination based on the geometric concept proposed by Bartlett and Hall [10] using static sessile drop imaging.

3.2. Powder purity

Inductively coupled plasma-mass spectroscopy (ICP-MS) was performed on the as-obtained Y$_2$O$_3$ powders in order to reveal the level of impurity deviation between powder P$_1$ and P$_2$. Impurity value levels in parts per million (ppm) were obtained for both powders. In case of powder P$_1$ this was less than 62 ppm Na. An exact Na content was not available for this powder, although it is expected to have a lower Na content in comparison with the other powder. Furthermore 29 ppm Si, 19 ppm K, 17 ppm Ca and 5 ppm Cu were detected. Alternatively, powder

Fig. 5. Detail BSE-image of the interface selected for EPMA measurements after contact angle wetting between Y_2O_3 substrates based on powder P_2 and a liquid Fe-Cr drop; Fe-9 wt.% Cr (Fig. 5(a)) and Fe-9 wt.% Cr-0.5 wt./% Si (Fig. 5(b)).

Fig. 6. Cumulative frequency curves as a function of particle size observed for the as-prepared Y_2O_3 powder P_1 and P_2. Additional illustration of the statistical fractions D_{10}, D_{50} and D_{90}.

P_2 contains 62 ppm Na, 30 ppm Si, 38 ppm K, 286 ppm Ca, 11 ppm Cu. Those relatively high levels of impurities and the 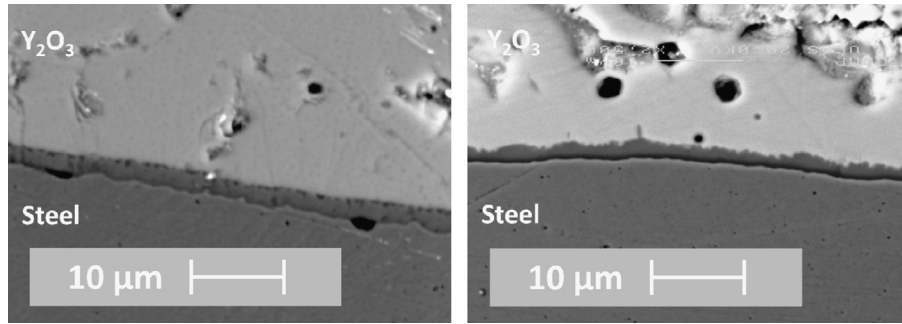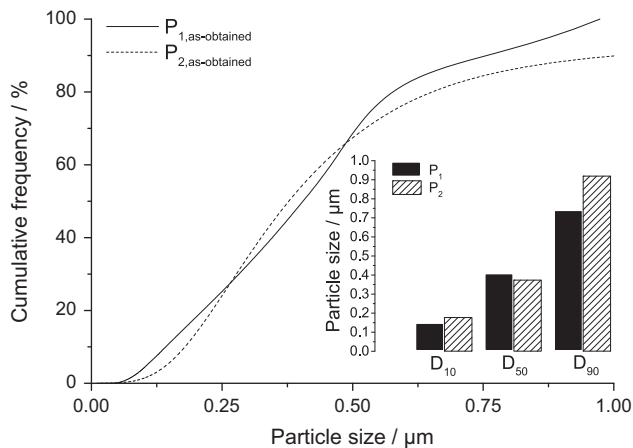differences in impurity level between both powders are investigated for their possible effect on the observed wettability.

3.3. Ceramic substrate preparation

3.3.1. Densification

After compressing the Y_2O_3 nano-powder into cylindrical shaped substrates, green body densification was obtained during sintering. The substrates densification during isothermal sintering at 1600 °C as a function of sintering time is presented in Fig. 8, for powders P_1 and P_2 in the as-obtained condition.

Fig. 8 allows concluding that during green body sintering, the degree of porosity decreases. In case of powder P_2, nearly complete densification is obtained after 2 h sintering since a theoretical density (TD) value of 98.1% is achieved. In case of the substrates based on powder P_1, densification seems to be more difficult resulting in a TD value of 80%, even for prolonged sintering times. Moreover, the sintering speed expressed as $\Delta TD/\Delta t$ (%/min) is at the start of sintering approximately 10 times faster for the powder P_2 as compared to the powder P_1. The main reasons for this observed difference for powders P_1 and P_2 are assumed to be twofold.

It has been reported in literature [35] that impurities such as Ca and Si contribute to the densification, it has to be stated that powder P_2 has a significantly higher Ca content. Secondly, also powder roughness might play a role. Increased powder roughness results in more inter-agglomerate porosity, which consequently allows more volume shrinkage and increased calcinations. As demonstrated in the next section, differences in powder roughness between the two powders were observed.

3.3.2. Surface roughness

As surface roughness has an impact on the contact angle formation at the S/L interface, the contact surfaces were polished after sintering, and this before determination of the contact angle. Fig. 9(a) and (b) presents SEM images of the sintered cylindrical substrates based on powder P_1 with a final TD of 77.1% before and after polishing.

From Fig. 9 it can be concluded that the surface structure of the P_1 compressed substrate sintered up to 77.1% TD, differs significantly before polishing (Fig. 9(a)) and after polishing (Fig. 9(b)) with 30 μm diamond paste. The SEM image of the ceramic structure after polishing reveals a structure with internal porosities being far from dense, as well as the presence of several surface cracks. Also, during sample preparation, depending on the micronite size of the diamond paste used, the sintered cylindrical work piece was more damaged and contaminated after final polishing with 9 μm paste compared to the use of a 30 μm paste. The internal porosities appearing after polishing can be caused by the initial agglomeration state of the as-obtained powder P_1. The observed porous structure after removal of the first material layers by polishing is most probably caused by the agglomeration state of the starting powder, inducing a more irregular packing of the particles. Based on these results, it can be concluded that elemental crystallite aggregation and consequently powder agglomeration leads to increased surface roughness R_s. The roughness factor calculations based on Eqs. (2) and (3) in Section 2.2.2 are 14.05 and 7.7 for the P_2 and P_1 as-obtained powder, respectively. The calculated surface roughness of the powder P_2 seems to be the double of the value calculated for the powder P_1. The values obtained assume that the powder P_2 is more rough leading to a higher agglomeration degree and consequently higher porosity compared to the powder P_1. Based on the presented
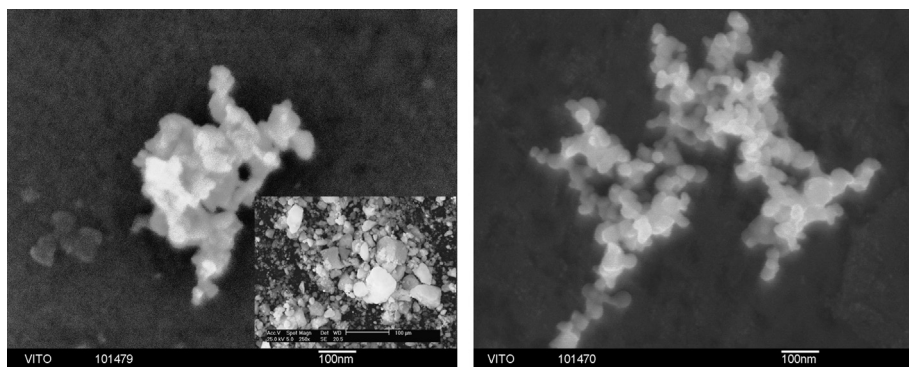
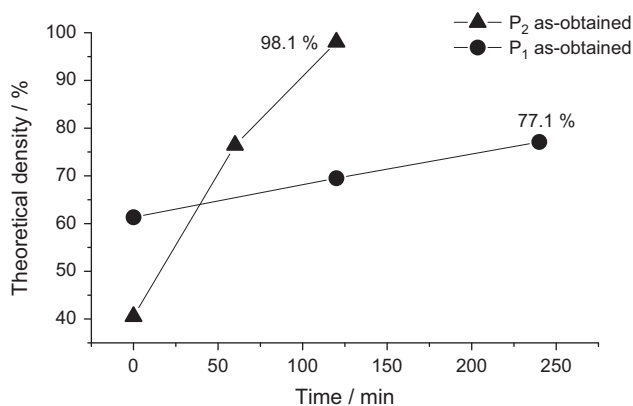Fig. 7. SEM images of the as-obtained Y_2O_3 nano-powder P_1 and P_2.

Fig. 8. Densification during isothermal sintering as a function of the sintering times for Y_2O_3 in the as-obtained condition.

observations for powder P_1, all contact angle measurements were performed on unpolished ceramic substrate.

3.3.3. Powder shrinkage during sintering

Horizontal powder dilatometry (HPD) was performed on cylindrical shaped bodies in order to investigate the shrinkage in length dL/L_0 (%) of Y_2O_3 powder P_1 and P_2 as a function of sintering time (min) at isothermal sintering temperatures of 1600 °C. Fig. 10 presents the shrinkage as a function of time, a typical sintering routine is also depicted in the figure.

From Fig. 10 it can be concluded that maximum shrinkage is represented by the difference in dL/L_0 and turns out to be about 17% for powder P_2 after the applied heating cycle, while the shrinkage level for the powder P_1 is about 6.5%.

3.3.4. Iron–chromium casts

The nominal elemental composition of the Fe–Cr alloys was investigated using ICP-MS. The nominal elemental composition in ppm detected for the electrolytic iron batches was 9 ppm carbon (C), 1 ppm manganese (Mn), 20 ppm silicon (Si), 7 ppm phosphor (P), 4 ppm sulfur (S), 1 ppm nickel (Ni), 23 ppm nitrogen (N), 6 ppm molybdenum (Mo), 4 ppm copper (Cu), and 1 ppm Cr. No elemental traces of vanadium (V), niobium (Nb) and oxygen (O) were found. In total it can be concluded that the total impurity content of the electrolytic iron matrix was 56 ppm.

3.4. High temperature wetting behavior

3.4.1. Determination of capillary lengths

For the experimental alumina and yttria/ferrous alloy systems with Cr addition studied; drop radii, drop heights and capillary lengths were measured analyzing the solidified drop images. All values are presented in Table 1.

Considering the yttria/ferrous alloy system we have studied, we can conclude the following. In all cases of the yttria/ferrous alloy system with Cr addition, the drop radius is slightly larger compared to the CL-value and independently of powder purity. The same conclusion can be made for the alumina/ferrous alloy system. The drop radius is in all cases slightly smaller compared to the drop height. For electrolytic iron without Cr addition in contact with the pressed P_1 substrate, the drop radius is slightly higher compared to the drop height and its CL.

Overall, we can conclude that the influence of gravitational forces can be neglected in the contact angles formation for the yttria/ferrous alloy system with Cr addition. This, independently of powder purity, as the difference in drop radius and CL-value is not significant high but minimal. It was referred in literature that gravitational effects dominate for drops who's drop radius largely exceeds the CL-value ($R \gg CL$). Low gravitational force influence is also confirmed by drop curvature seen the images of experimental contact angles.

For capillary length calculations described in literature, we refer to the work of Berg [36] in which the surface tension of liquid iron against the vapor phase of air at elevated temperature (1530 °C) was determined to be 1700 mN/m. In case of high-purity vacuum-melted iron, it is described that the surface tension is in the range above > 1000 mN/m [37].

Final capillary length can be estimated by the formula = square root(surface tension/($g \times \rho$)). Based on a surface tension value between 1000 and 1700 mN/m, the CL calculated varies between 3.6 mm and 4.69 mm. This for a value $g = 9.81$ m/s^2 and density = 7860 kg/m^3. This is in accordance to the experimental CL-value measured for the yttria/ferrous alloy system.

3.4.2. Influence of the chromium content

Fig. 11 depicts the observed contact angles θ_c as a function of Cr-content (0–20 wt% Cr) measured for substrates prepared with Y_2O_3 nano-powder in contact with binary Fe–Cr alloys,
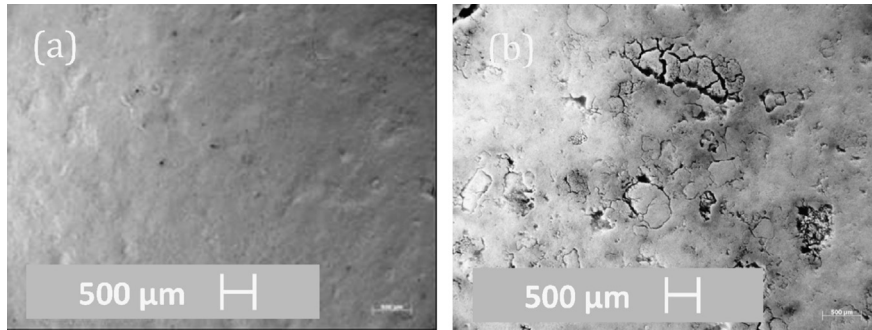
Fig. 9. Secondary electron (SE)-micrographs of the P_1 sintered substrates (77.1% *TD*) before (a), and after (b) polishing with 30 μm diamond paste.
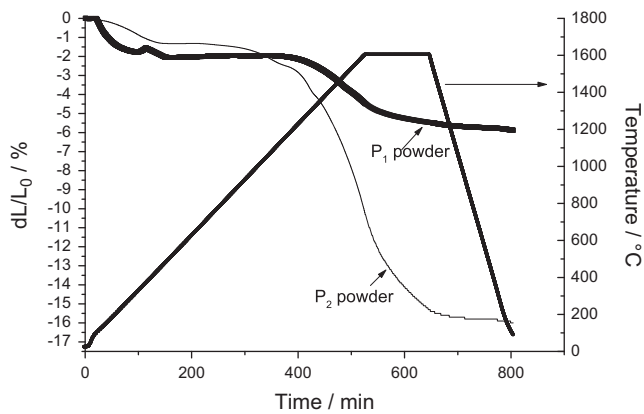

Fig. 10. Length shrinkage (dL/L_0) as a function of sintering time for Y_2O_3 powders P_1 and P_2, and applied heating cycle.

Table 1
Drop radii, drop height and capillary length for the alumina and yttria/ferrous–Cr alloy systems based on the experimental images for the droplets after solidification.

Fe–Cr alloy	Drop radius (mm)	Drop height (mm)	Capillary length (mm)
Argon Al_2O_3			
0	3.63	< 4.1	> 3.18
2.5	3.95	< 4.21	> 3.51
5	3.93	< 4.14	> 2.95
9	3.6	> 3.36	> 3.07
12	4.07	> 3.90	> 3.61
14	4.05	> 3.53	> 3.48
20	4.04	> 3.75	> 3.16
Argon P1			
0	3.61	> 3.31	> 3.14
2.5	2.53	< 4.01	< 2.98
5	3	< 3.65	> 2.8
9	3.78	= 3.78	> 2.91
12	3.97	< 4.12	> 3.24
14	3.66	< 3.87	> 3.05
20	3.26	< 4.31	> 2.8
Argon P2			
0	3.4	< 4.07	> 3.14
2.5	3.72	< 3.86	> 2.37
5	3.87	< 4.46	> 3.34
9	3.36	< 3.8	> 3.04
12	3.72	< 3.94	> 2.55
14	3.39	< 3.74	> 2.75
20	3.72	< 4.25	> 2.87

under protective atmosphere. A comparison is made with Al_2O_3 under both vacuum conditions and protective argon atmosphere.

From Fig. 11 it can be observed that in case Al_2O_3 substrates are in contact with the binary Fe–Cr steel melt, the S/L interactions dominate at the interface. Consequently, contact angles below 90° are obtained resulting in good wet ability between Al_2O_3 and the liquid Fe–Cr steel melt under argon atmosphere, especially at higher Cr-content. When varying the atmosphere above the S/L interface, vacuum or argon, it was observed that vacuum conditions lowered the wettability of the ceramic alumina. When keeping in mind the final goal, i.e., the addition of Y_2O_3 to a liquid steel melt, as well as considering the results of Al_2O_3 wetting only tests under protective argon atmosphere were undertaken in case of Y_2O_3.

The results presented in Fig. 11 indicate that the wettability between Y_2O_3 nano-powder substrates and liquid Fe–Cr melts under argon atmosphere is rather weak, as the observed contact angles θ_c exceed values over 90° in all cases. A second observation that can be made is that a higher powder purity does not seem to cause a significant improvement. On the contrary it is rather detrimental for the wettability between Y_2O_3 nano-powder and liquid Fe–Cr steel melts. Therefore, it can be concluded that the wettability of highly pure Y_2O_3 in

contact with Fe–Cr steel melts is rather low and dominated by interfacial L/L interactions. No clear correlation is observed between the amount of Cr added to the iron melt and the contact angles observed within the range of Cr concentrations studied. Nevertheless, some tendency exists that the wettability of Fe–Cr alloys onto Y_2O_3 substrates decreases with increased amount of Cr. The only composition at which the wettability seems to be satisfying is at the test condition of pure iron without any Cr addition. In case of the powder P_1 the contact angle remains at 95°. While in the case of low-purity powder P_2 the contact angle turns out to be exactly 90° which makes the case of pure electrolytic iron in contact with a less pure powder 'a close call'. In case of the 9 wt% chromium binary alloy, which is the basic matrix of commonly structural
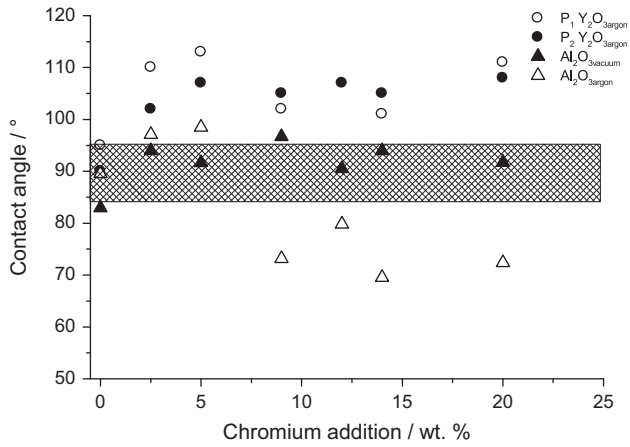
Fig. 11. Contact angle values θ_c as a function of increased Cr addition for Y_2O_3 nano-powders in contact with binary Fe–Cr (0–20 wt% Cr) alloys; experiments under protective argon atmosphere. A comparison is made with Al_2O_3 under vacuum and under protective argon atmosphere.
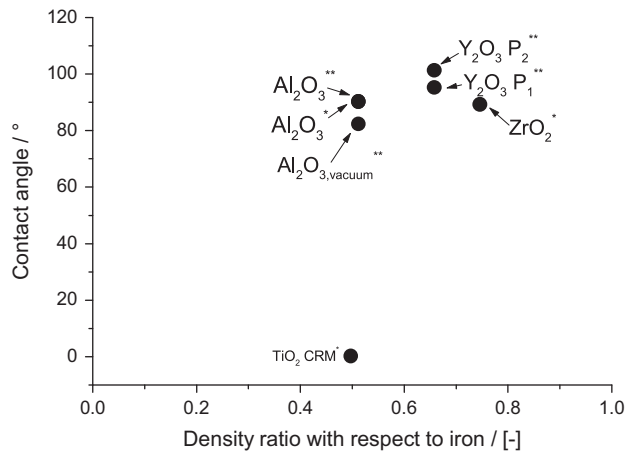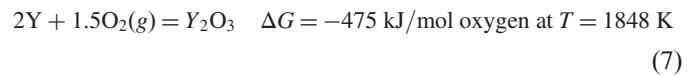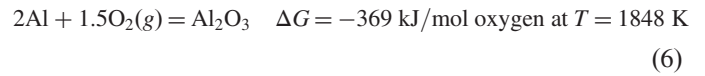

Fig. 12. Contact angle values θ_c of oxides as a function of density ratio with respect to electrolytic iron ([38]*, [39]**).

materials used for nuclear applications as well as for classical power production units based on cokes, steam and gas, it is clear that the wettability towards Y_2O_3 nano-powder is low. Low wettability of the Y_2O_3 ceramic solids can be mainly explained by the fact that metals, glasses and ceramics are typical 'hard solids'. The chemical bonds at atomic level are typically covalent, ionic or metallic and those bonds are relatively strong. As a consequence, a large interfacial surface energy or low wetting behavior between the alloy and the ceramic is expected and hereby experimentally confirmed.

In Fig. 12, θ_c is presented as a function of density ratio (with respect to electrolytic iron) for both Y_2O_3 powders investigated and compared to literature values for other oxides such as titanium oxide (TiO_2), zirconium oxide (ZrO_2) and Al_2O_3 [38,39]. All contact angles are measured under protective atmosphere, unless otherwise stated. Contact angle values were obtained during studies performed at the center for research in metallurgy (CRM*) and the Flemish institute for technological research (VITO**).

From Fig. 12, it can be derived that for all oxides investigated, contact angles close to 90° are observed in contact with electrolytic pure iron. Only in case of TiO_2 in contact with pure iron, perfect wetting is reported. There is no correlation observed between the θ_c value and the density ratio with respect to iron.

The free energy of formation ΔG for Y_2O_3 as a function of temperature is larger in absolute value compared to Al_2O_3 and all other oxides, see Eqs. (6) and (7), making yttria thermodynamically the most stable oxide [40].

$$2Al + 1.5O_2(g) = Al_2O_3 \quad \Delta G = -369 \text{ kJ/mol oxygen at } T = 1848 \text{ K} \tag{6}$$

$$2Y + 1.5O_2(g) = Y_2O_3 \quad \Delta G = -475 \text{ kJ/mol oxygen at } T = 1848 \text{ K} \tag{7}$$

Practically this means that all oxides different from Y_2O_3 will more 'easily' de-bond and will react more easily with the melt phase compared to yttria. This is in line with the experimental observations on the wettability between the described oxides and ferrous alloys.

3.4.3. Influence of silicon content

Finally, the effect of Si on the wettability of Fe–Cr melts onto Y_2O_3 pressed substrates is investigated. Fig. 13 depicts the influence of increased Si content on contact angles formation of liquid steel melts (9 wt% Cr) onto Y_2O_3 substrates.

From Fig. 13 it can be concluded that 9 wt% Fe–Cr alloys containing an increased amount of Si, show improved wettability. It seems that the addition of Si increases the interactions at the S/L interface or, otherwise stated, decreases the surface tension between solid ceramic and liquid steel. Although statistics are poor due to the limitation in data, an extrapolation of the curve indicates it might be possible to lower the contact angle from 102° to 90° by increasing the Si content up to 0.74 wt% for the low-purity powder P_2. In case of the high purity powder P_1 unrealistic high Si contents should be added in order to lower the contact angle to similar values.
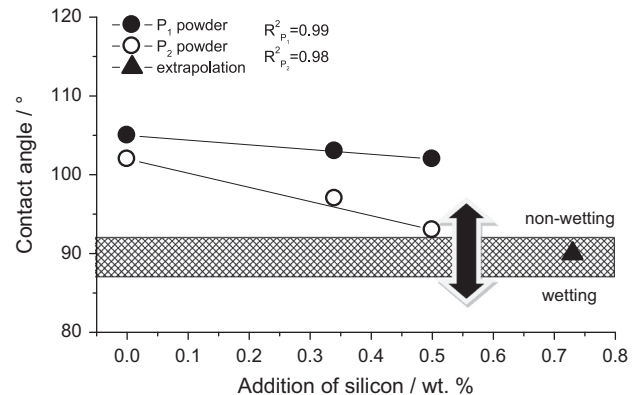

Fig. 13. Contact angle θ_c as a function of silicon content for 9 wt% chromium alloys.

3.5. Substrate analysis

Optical stereo microscopy (OSM) is used to evaluate the color formation of the Y_2O_3 ceramic work pieces after hot stage contact angle wetting. Obtained OSM images after wetting tests of both Y_2O_3 powders P_1 and P_2 in contact with Fe–Cr steels alloyed with 0, 2.5, 5 and 20 wt% Cr, as well as after sintering, are presented in Fig. 14.

Observing the images presented in Fig. 14, different colorization is seen for the pressed and sintered P_1 and P_2 plates in contact with Fe–(0–2.5–5–20 wt.% Cr) alloys. Most probably different elemental diffusion and interaction at the S/L interface cause this effect, correlated to powder purity.

The pressed powder plates, in case of the pure powder P_1 as well as impure powder P_2 originally appeared white after pressing. After sintering under air, a white–yellow color on the impure P_2 powder pressed substrates appeared, for the pure powder P_1 no color change formation was observed. The Y_2O_3 pressed substrates based on powder P_2, reveal dark spots ('islands') throughout the ceramic substrate sample, after sintering in air. This color changing phenomenon is well-known as indicator that yttria's stoichiometry alters towards lower oxygen content according to the following reaction in the following equation [14,41,42]:

$$Y_2O_3 = xO + Y_2O_{(3-x)} \qquad (8)$$
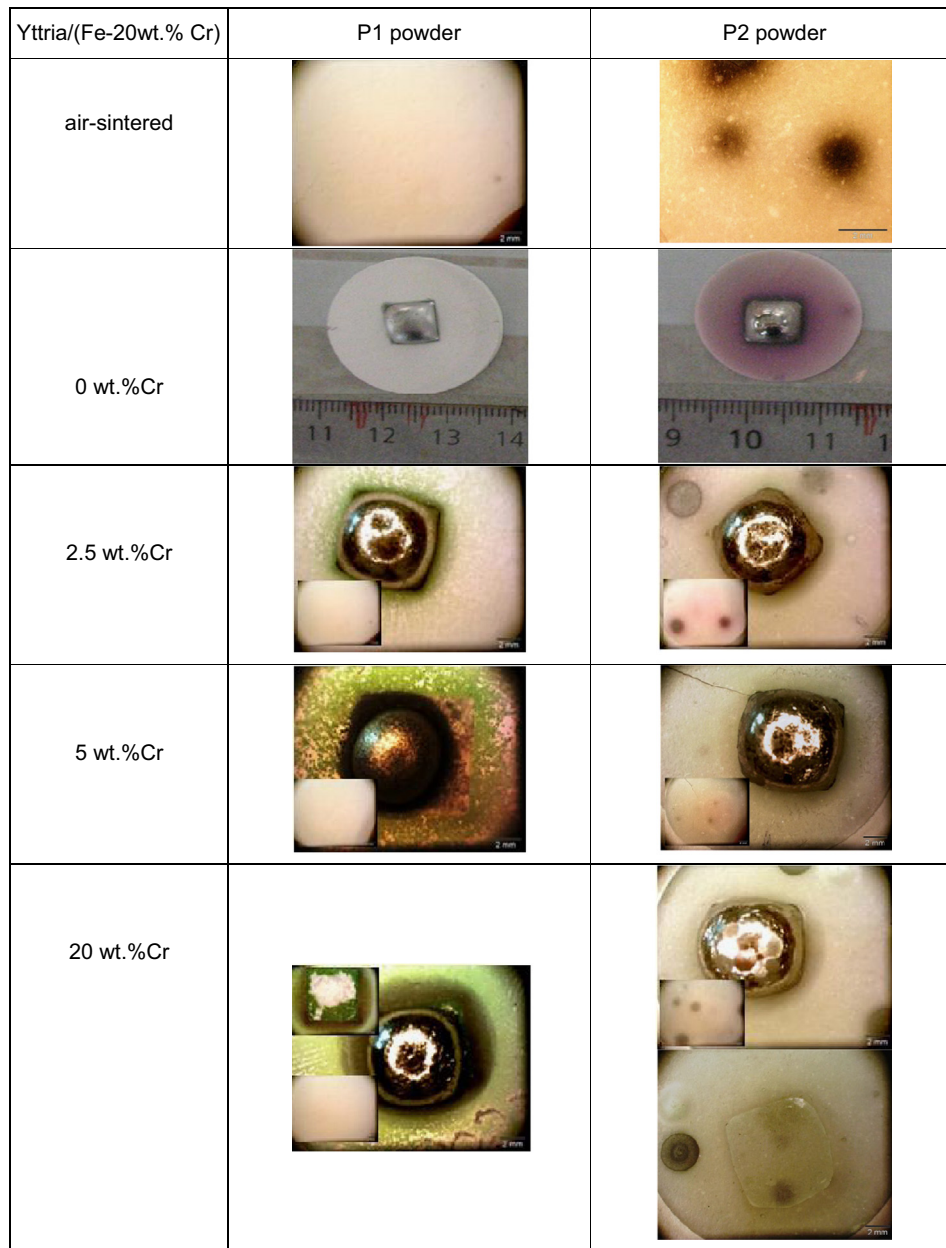
Fig. 14. OSM depicting the colorization of Y_2O_3 ceramic substrates after air sintering and after wetting experimentation between powders P_1 (a) and P_2 (b) in contact with iron drops and Fe–Cr (2.5–5 and 20 wt%) alloys. Front view of the drop in contact with the substrate, visualization under the drop is presented left side up, back view is presented left side under. (For interpretation of the references to color in this figure, the reader is referred to the web version of this article.)

No dark spotting was observed after air sintering the high-purity P_1 pressed substrates. After hot stage contact angle wetting, in case of the composition Fe–2.5 wt% Cr, a more reddish color is observed at the interaction interface where the alloy drop makes contact with the impure powder P_2 pressed plates. The red color penetrates throughout the ceramic plate, as indicated on the small figure presented in the left corner of the respective OSM image displayed. With increased amount of Cr addition (5–20 wt%), it is seen that the red colorization diminishes in intensity in case of contact with the impure powder P_2. The red color pattern clearly becomes dominated by the green color with increased amount of Cr added. Besides the substrate's red color formation, some dark color seem to spread around the area of contact. Discussed color changes are presented in Fig. 15.

In case of the composition Fe–2.5 wt% Cr in contact with powder P_1, a slight green color dominates. For an increased amount of Cr addition (5 and 20 wt%), a bright green color becomes dominant and more intense. Similar to powder P_1, besides the substrate's green color formation, the dark color spread around the area of contact is also seen, see Fig. 15. For the composition Fe–0 wt.% Cr in contact with Y_2O_3 pressed substrates, only in case of the powder P_2 a pronounced and deep dark red color spreads out over the ceramic substrate.

3.6. Reaction chemistry at the S/L interface

To understand the reaction chemistry which might play an important role in the wettability at the S/L interface of the impure powder P_2, suggested by OSM observations, EPMA was used to identify and localize the compound related to the color formation. With the final goal being the production of high Cr dispersed steels (9 wt% or higher), it was decided to focus on the reaction chemistry of the Fe–9 wt% Cr system in this work. The resulting EPMA mappings for the samples with identification (ID) Fe–9 wt% Cr and Fe–9 wt% Cr–0.5 wt% Si are presented in Fig. 16 (left column and right column),

respectively. In all cases, the samples were scanned top down, i.e., in direction ceramic substrate to steel drop.

From Fig. 16 it is observed that an increased segregation takes place at the S/L interface, for the Fe–9 wt% Cr alloy. With increased amount of Cr-content present in the liquid Fe–Cr drop, depletion of Cr from the Fe drop is observed with an excess in Cr concentration at the S/L interface.

For the P_1 yttria/Fe–9 wt% Cr system, we assume the following chemical reactions took place at the wetting interface. We assume it plausible and not unlikely that, in combination with free oxygen (Eq. (8)), Cr reacts with O at the interaction interface and that a Cr_2O_3 layer (with its characteristic green color) has formed at the interface according to the following reaction:

$$2Cr + 3O \rightarrow Cr_2O_3 \qquad (9)$$

Seen the EPMA images, the interaction layer thickness is in the order of 4–5 μm. Most probably, thickness of the interaction layer will increase with increased Cr-content. As Cr can be seen as active metal element in the liquid droplet phase, wetting could be promoted. Nevertheless insufficient reaction control can lead to incomplete bonding, resulting in interface degradation. Or in this case, excessive reaction on the other hand, and consequent reaction layer thickening can also lead to a degradation of the bond [19]. This would explain the reduced wettability with increased Cr-content observed for the yttria/ferrous alloy systems, confirmed by the fact that for those alloys the solidified drops easily detached from the substrate after cooling. In general, crack formation at the interaction interface is not directly seen.

In case of the impure powder P_2, the green color is slightly dominated by a red coloring for lower Cr-contents caused by formation of an Fe–Y–Ca–Si rich compound. In another study, the wettability between Y_2O_3 and Fe–0 wt% Cr is studied in more detail [29]. The Fe–Y–Ca–Si rich compound being confirmed by the enhanced Ca and Si levels at the interaction interface and depleting the small islands formed in the yttria substrate. As Cr-content increases, the green color becomes
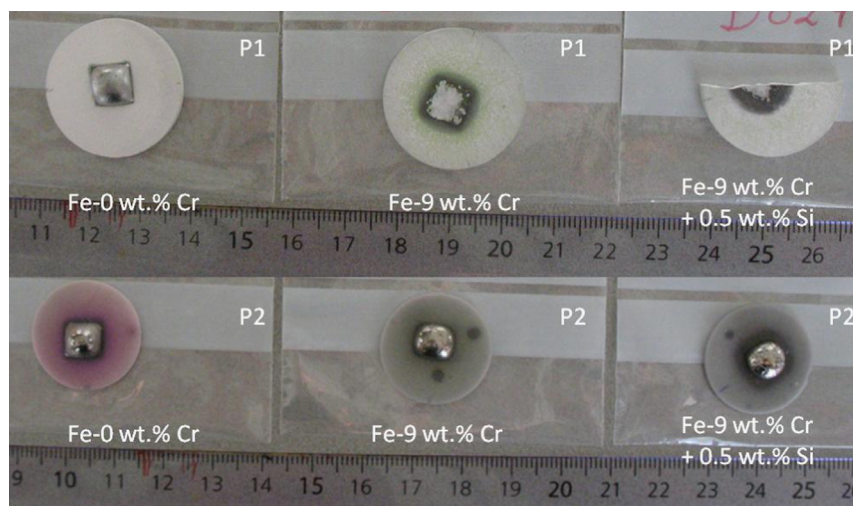

Fig. 15. Macro-imaging of the samples Fe–0 wt% Cr, Fe–9 wt% Cr (+0.5 wt% Si) in contact with powder P_1 and P_2 pressed substrates. (For interpretation of the references to color in this figure, the reader is referred to the web version of this article.)
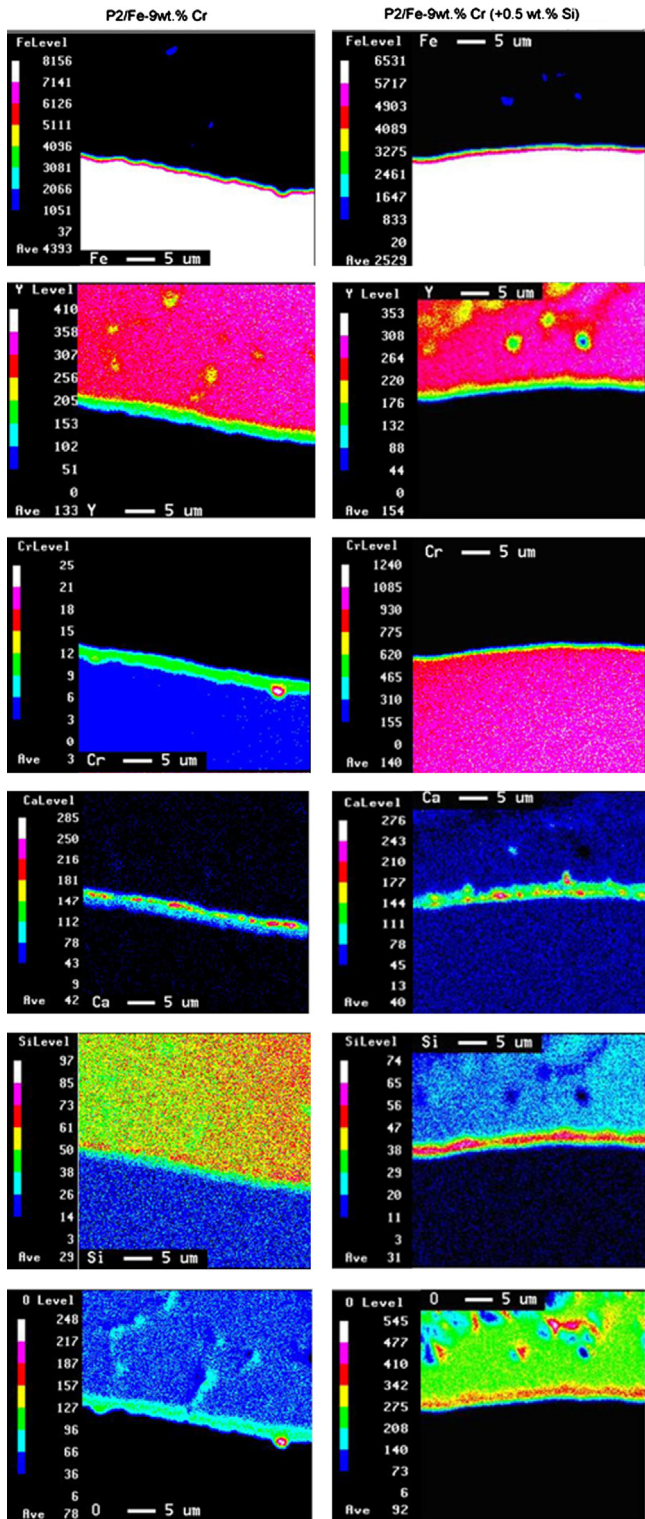
Fig. 16. Elemental mapping of Y, Fe, Ca, Si, C and O at the interface of contact between the low-purity Y_2O_3 powder P_2 and Fe–9 wt% Cr (+0.5 wt% Si) alloys. (For interpretation of the references to color in this figure, the reader is referred to the web version of this article.)

dominant and seems to outvote the red colour with increased amount of Cr-content.

In case of both powders P_1 and P_2, seen the enhanced Cr and Y levels at the interface layer of contact, as can be derived from the EPMA images presented in Fig. 16, it is not unlikely that simultaneously the following reaction mechanism took place:

$$Y_2O_3 + Cr \rightarrow CrYO_3 + Y \qquad (10)$$

Only the EPMA images for the powder P_2 are presented for the wetting conditions Fe–9 wt% Cr, nevertheless the signals for powder P_1 for the same wetting conditions are available. During the formation of a chromium yttrium compound, the release of free Y is confirmed by the thin Y layer formed closely to the interface layer of contact between the drop and ceramic substrate. A deep crater beneath the drop, with a depth of 2.5 μm, being an incentive for the observed interaction layer. Si additions to the melt reduces the crater depth, and consequently the thickness of the interaction layer.

The black coloration is typically caused by yttria altering its stoichiometry to lower oxygen content. The substrate's stoichiometry probably changes at the interaction interface during contact angle wetting as a result of the following reaction:

$$(1-x/3)Y_2O_3 + 2(x/3)Y = Y_2O_{(3-x)} \qquad (11)$$
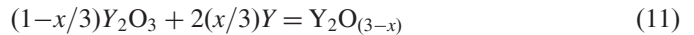
Nevertheless, interesting is that, with addition of 0.5 wt% Si to a Fe–9 wt% Cr liquid drop, the segregation of Cr to the S/L interface is 'retained', confirmed by the concentration level of elemental Cr measured in the drop phase and Si seeming to diffuse/penetrate (T_m Si=1410 °C) to the S/L interface. It is clear that in case of Fe–9 wt% Cr, a segregated Cr layer dominates at the interface, resulting in decreased wettability between yttria and the Fe–Cr liquid drop. Nevertheless, with the addition of 0.5 wt% Si to the liquid Fe drop containing a constant amount of 9 wt% Cr, the L/L interactions at the S/L interface decreases resulting in improved wettability. It is clear that the addition of Si has an impact on the S/L interactions resulting in a decreased surface tension and improved wettability. Si seems to be more pronounced present at the interaction interface, in addition, Ca, being a major impurity of powder P_2, enriches at the S/L interface.

4. Conclusion

In this study, high-temperature wetting behavior between Y_2O_3 in contact with liquid Fe–Cr alloys under argon atmosphere has been investigated using the static sessile drop method. Two powders P_1 and P_2 with different purity content are thoroughly evaluated on their wettability in contact with Fe drops containing different Cr-contents.

Contact angles above 90° were encountered, confirming the high interfacial energy applying at the S/L interface between Y_2O_3 in contact with liquid Fe–Cr alloys. The contact angle results observed for electrolytic pure Fe, without Cr, differs significantly from those obtained for the Fe–Cr alloys. Only for the test condition of pure electrolytic iron in contact with Y_2O_3 without Cr addition, the contact angles (θ_c) were found to approach 90° in all cases (P_1 and P_2). In case Si was added to a 9 wt% Cr alloy, it is observed that the addition of Si enables to lower the contact angle value. The largest decrease in contact angle values with Si addition to an Fe–Cr alloy drop, was observed for the impurest powder P_2.

OSM-imaging elucidated the color changes of the ceramic substrates at the interaction interfaces after wetting. An overall green color was detected at the interface for the high-purity powder P_1 in contact with high-chromium alloyed steel. A more reddish color was seen for the less pure powder in contact with Fe–Cr drops. For the latter, it must be stated that the red color becomes dominated by the green color when Cr-content increases.

The EPMA measurements reveal a possible relation between the color change and powder purity, and explains the deviation in contact angles observed between both powders. In case of the impure powder P_2, an increased Cr segregation is observed in contact with the Fe–9 wt% Cr alloys while a Ca and Si rich layer stimulates the wettability between the ceramic and the Fe–9 wt% Cr (+Si) alloy.

To further elucidate the interactions between electrolytic iron drops and yttria, another study [29] details and discusses the interaction between electrolytic Fe drops and impure Y_2O_3 powder parallel to its casting. In that study, it is clearly confirmed evaluating the EPMA measurements that for electrolytic Fe in contact with ceramic Y_2O_3 substrates, based on impure powder, the formation of a Si and Ca rich compound is observed at the interface. This indicates the possible and positive effect of elements being active at the interaction surface. The addition of surface active elements such as Si can be an alternate experimental set-up that will be further discussed in another part of this work [30] in which the advances in the development of corrosion and creep resistant nano-dispersed ferrite/martensite alloys using rapid solidification processing techniques are discussed.

Acknowledgments

References

[1] H. John, H. Hausner, Wetting of aluminium oxide by liquid aluminium, International Journal of High Technology Ceramics 2 (1986) 73–78.

[2] D.T. Livey, P. Murray, The wetting properties of solid oxides and carbides by liquid metals, in: Proceedings of the 2nd Plansee Seminar, Reutte/Tirol (1955) pp. 375–404.

[3] R.D. Carnahan, T.L. Johnston, C.H. Li, Some observations on the wetting of Al_2O_3 by aluminium, Journal of the American Ceramic Society 41 (1958) 343–347.

[4] S.M. Wolf, A.P. Levitt, J.L. Brown, Whiskermetal matrix bonding, Chemical Engineering Progress 62 (1966) 74–78.

[5] J.J. Brennan, J.A. Pask, Effect of nature of surfaces on wetting of sapphire by liquid aluminium, Journal of the American Ceramic Society 51 (1968) 569–573.

[6] J.A. Champion, B.J. Keene, J.M. Sillwood, Wetting of aluminium oxide by molten aluminium and other metals, Journal of Materials Science 4 (1969) 39–49.

[7] P. Sebo, J. Ivan, L. Taborsky, A. Havalda, Benetzung von Al_2O_3 durch flüssiges aluminium, Kovoré Materialy 2 (1973) 173–180.

[8] W.T. Köhler, E. Van Rensen, K. Sahm, Entwicklung faserverstärkter Verbundwerkstoffe mitt metallischer matrix, BMFT-Forschungsbericht T 73 (1973) 73–74.

[9] W. Dawihl, H. Federmann, Einfluβ metallischer Aufdampfschichten auf das Benetzungsverhalten von Reinstaluminium auf Al_2O_3-Unterlagen, in: Fachberichte der Tagung Verbundwerkstoffe, Konstanz (1974) pp. 450–468.

[10] R.W. Bartlett, J.K. Hall, Wetting of several solids by Al_2O_3 and BeO liquids, American Ceramic Society Bulletin 44 (1965) 444–448.

[11] R.M. Balestra, S. Ribeiro, S.P. Taguchi, F.V. Motta, C. Bormio-Nunes, Wetting behaviour of Y_2O_3/AlN additive on SiC ceramics, Journal of the European Ceramic Society 26 (2006) 3881–3886.

[12] S.P. Taguchi, F.V. Motta, R.M. Balestra, S. Ribeiro, Wetting behavior of SiC ceramics Part II—Y_2O_3/Al_2O_3 and Sm_2O_3/Al_2O_3, Materials Letters 58 (2004) 2810–2814.

[13] O. Dezellus, N. Eustathopoulos, Fundamental issues of reactive wetting by liquid metals, Journal of Materials Science 45 (2010) 4256–4264.

[14] S. Barzilai, M. Aizenshtein, E. Shapiro-Tsoref, N. Froumin, N. Frage, Interface interaction and wetting in the Y_2O_3/(Al–Cu–Y) system, International Journal of Adhesion & Adhesives 27 (2007) 358–361.

[15] O. Dezellus, N. Eustathopoulos, Fundamental issues of reactive wetting by liquid metals, Journal of Materials Science 45 (2010) 4256–4264.

[16] N. Sobczak, M. Singh, R. Asthana, High-temperature wettability measurements in metal/ceramic systems—some methodological issues, Current Opinion in Solid State & Materials Science 9 (2005) 241–253.

[17] J.S. Duncan, Introduction to Colloid and Surface Chemistry, third edition, Butterworths, England (1980) 127-142.

[18] J.X. Zhang, R.S. Chandel, H.P. Seow, International Journal of Modern Physics B 16 (2002) 50.

[19] K. Nakashima, H. Matsumoto, K. Mori, Effect of additional elements Ni and Cr on wetting characteristics of liquid Cu on zirconia ceramics, Acta Materialia 48 (2000) 4677–4681.

[20] R. Lindau, A. Môslang, M. Schirra, P. Schlossmacher, M. Klimiankou, Journal of Nuclear Materials 307–311 (2002) 769–772.

[21] Z. Oksiuta, N. Baluc, Journal of Nuclear Materials 374 (2008) 178–184.

[22] A. Alamo, J.L. Bertin, V.K. Shamardin, P. Wident, Journal of Nuclear Materials 367–370 (2007) 54–59.

[23] C. Degueldre, S. Conradson, W. Hoffelner, Computational Materials Science 33 (2005) 3–12.

[24] S. Ukai, T. Nishida, H. Okuda, M. Fujiwara, K. Asabe, Journal of Nuclear Science and Technology 34 (1997) 256.

[25] S. Ukai, T. Yoshitake, S. Mizuta, Y. Matsudaira, S. Hagi, T. Kobayashi, Journal of Nuclear Science and Technology 36 (1999) 710.

[26] R.L. Klueh, J.P. Shingledecker, R.W. Swindeman, D.T. Hoelzer, Journal of Nuclear Materials 341 (2005) 103–114.

[27] I.S. Kim, J.D. Hunn, N. Hashimoto, D.L. Larson, P.J. Maziasz, K. Miyahara, E.H. Lee, Journal of Nuclear Materials 280 (2000) 264.

[28] W.B. Eisen, B.L. Ferguson, R.M. German, R. Iacocca, P.W. Lee, D. Madan, K. Moyer, H. Sanderow, Y. Trudel, Powder Metal Technologies and Applications, Mechanical Alloying, vol. 7, ASM Handbook, American Society for Metals, 1998, p. 208.

[29] K. Verhiest, S. Mullens, J. Paul, N. DeWispelaere, S. Claessens, A. DeBremaecker, K. Verbeken, Comprehensive study on the sintering behaviour of yttria nano-powder in contact with electrolytic iron using the rapid solidification processing technique, unpublished results, in preparation.

[30] K. Verhiest, S. Mullens, J. Paul, N. DeWispelaere, S. Claessens, A. DeBremaecker, K. Verbeken, Advances in the development of corrosion and creep resistant nano-yttria dispersed ferritic/martensitic alloys using the rapid solidification processing technique, unpublished results, in preparation.

[31] C. Takai, M. Tsukamoto, M. Fuji, M. Takashashi, Control of high solid content yttria slurry with low viscosity for gelcasting, Journal of Alloys and Compounds 408–412 (2006) 533–537.

[32] K.A. Gschneider, Rare Earth Alloys, A Critical Review of the Alloy Systems of the Rare Earth, Scandium and Yttrium Metals, D. Van Nostrand Company INC., Princeton, New Yersey, 1961.

[33] ⟨http://www.pdftop.com/ebook/callister+fe+cr+phase+diagram⟩.

[34] H.K. Bowen, Basic research needs on high temperature ceramics for energy applications, Materials Science and Engineering 44 (1980) 1–56.

[35] G.B. Granger, C. Guizard, Sintering behaviour and optical properties of yttria, Journal of the American Ceramic Society 90 (9) (2007) 2698–2702.

[36] J.C. Berg, An Introduction to Interfaces and Colloids, the Bridge to Nanoscience, World Scientific Publishing Co. Ptc. Ltd, Singapore, 2010.

[37] P.G. De Gennes, F. Brochard-Wyart, D. Quéré, Capillarity and Wetting Phenomena: Drops, Bubbles, Pearls, Waves, Springer Science+Business Media Inc, New York, 2004.

[38] Jean-Claude Herman, et al., Development of products with a fine distribution of ceramic nano- particles, HJN-State of the Art, Meeting Corus-CRM 16.03.2006, Haar-lem, Research Report 200505, 2006.

[39] S. Mullens, et al., Personal Communication.

[40] C.E. Wicks, F.E. Blocks, United States Bureau of Mines 605 (1963) 137.

[41] C. Tournier, B. Lorrain, F.Le. Guyadec, L. Coudurier, N. Eustathopoulos, Journal of Nuclear Materials 254 (1998) 215.

[42] N. Eustathopoulos, M.G. Nicholas, B. Drevet, in: Wettability at High Temperatures, first edition, Pergamon Press, Oxford (1999) 215-216.